Laser Physics Letters

Astro Ltd.

LETTER

Quantitative techniques for extraction of blood oxygenation from multispectral optoacoustic measurements

IOP Publishing | Astro Ltd
Laser Physics Letters
Laser Phys. Lett. **16** (2019) 116201 (12pp)
https://doi.org/10.1088/1612-202X/ab4dab

Letter

Quantitative techniques for extraction of blood oxygenation from multispectral optoacoustic measurements

V V Perekatova, P V Subochev, M Yu Kirillin, E A Sergeeva, D A Kurakina, A G Orlova, A S Postnikova and I V Turchin

Institute of Applied Physics, Russian Academy of Sciences, 46 Ulyanov Street, Nizhny Novgorod 603950, Russia

E-mail: ValeriyaPerekatova@gmail.com

Received 1 October 2019
Accepted for publication 8 October 2019
Published 30 October 2019

Abstract

We report on the comparison of two approaches to the reconstruction of oxygen saturation (StO_2) within blood vessels from multispectral optoacoustic (OA) measurements. The spatially-resolving approach is based on determination of the optical absorption coefficient μ_a from OA signal amplitudes, while the calibration-free approach is based on evaluation of the effective optical attenuation coefficient μ_{eff} derived from the in-depth OA signal decay. Both approaches were verified in phantom experiments as well as in *in vitro* and *in vivo* measurements. The results demonstrate good agreement of μ_a spectra derived from OA signal amplitudes with the published data indicating this approach to be preferable for the *in vivo* determination of StO_2. Reconstruction of μ_a spectra from the *in vivo* measured OA signal amplitudes in a rat yields StO_2 values of 0.57 ± 0.08 and 0.50 ± 0.07 for two veins of the thoracic spine. We demonstrate that for cost-effective measurements a dual-probing wavelength scheme can be employed instead of multiple wavelength probing. We found that the probing wavelength of 700 nm combined with a wavelength from the range of 850–1069 nm provides reconstructed StO_2 values close to the reference ones derived from multiple wavelength measurements in the entire range of 658–1069 nm.

Keywords: optoacoustic imaging, blood oxygen saturation (StO_2), fluence compensation

(Some figures may appear in colour only in the online journal)

1. Introduction

Biomedical optoacoustic (OA), or photoacoustic imaging [1, 2] is a hybrid modality combining the benefits of optical contrast and ultrasonic resolution. Due to high absorption of visible light in blood compared to surrounding biotissues, OA imaging is efficient for *in vivo* angiography [3–6]. At the same time, functional information provided by multispectral OA measurements of blood oxygen saturation (StO_2) is also important, since it significantly broadens the range of biomedical OA applications. Particularly, non-invasive mapping and volumetric determination of StO_2 in blood vessels has high potential for a number of clinical applications [3].

Two approaches to reconstruct StO_2 value from OA measurements are usually employed, both based on differences in absorption spectra of oxy- and deoxyhemoglobin. The first approach is based on extraction of blood oxygenation from OA signal amplitudes in blood vessels acquired at multiple optical wavelengths [7]. We will refer to it as 'amplitude measurement approach' (AMA). To quantify local concentrations of oxygenated and deoxygenated forms of hemoglobin in the given blood vessel one needs to determine optical absorption

coefficient $\mu_a(\lambda)$ within it. Extraction of μ_a spectra from the measured OA pressure requires information about distribution of optical fluence in biotissue for all probing wavelengths [8]. Due to complexity of light propagation in biological tissues, especially for complex-shaped probing beam [9], fluence distribution is unknown, which makes quantitative determination of optical absorption $\mu_a(\lambda)$ from OA measurements rather challenging [10]. Optical fluence can be approximated by an exponential decay function [11], or reconstructed from diffuse optical tomography [12], or derived from Monte Carlo modeling for complex illumination geometry [9], or obtained by combining the optical measurements with theoretical modeling [13]. In paper [14] the concentrations of oxyhemoglobin and deoxyhemoglobin were reconstructed from OA measurements in the wavelength range 740–1040 nm with a step of 10 nm by fitting the forward model of light propagation to the experimental data. The forward model included calculation of absorbed energy distribution using diffusion-based finite element light transport model for different concentrations of chromophores, calculation of initial pressure distribution and substitution of this initial pressure into forward wave equation. In paper [15] reconstruction of optical absorption coefficients from the amplitudes of OA signals acquired at multiple optical wavelengths was performed by minimizing the difference between the experimental and theoretical spectra of optical absorption in assumption of exponential fluence decay with the extinction coefficient equal to μ_a of blood.

The second approach to determine StO_2 is based on evaluation of the effective optical attenuation coefficient $\mu_{eff}(\lambda)$ from the OA signal decay in the given blood-containing vessel at multiple probing wavelengths [16]. The value of $\mu_{eff}(\lambda)$ depends on $\mu_a(\lambda)$ and the reduced scattering coefficient $\mu_s'(\lambda)$. The parameter μ_s' was reported to weakly depend on the oxygenation [17], and $\mu_a(\lambda)$ can be derived from the measured $\mu_{eff}(\lambda)$. We will refer to the second approach as 'decay measurement approach' (DMA). The main advantage of DMA is that it is calibration-free since $\mu_{eff}(\lambda)$ does not depend on the optical fluence. For calibration-free OA measurement of $\mu_{eff}(\lambda)$ in small and superficial blood vessels (<150 μm in diameter) optical wavelength range below 630 nm is usually employed [10, 18] since for this spectral band the light penetration depth into the tissue is small and $\mu_{eff}(\lambda)$ is high. Measuring $\mu_{eff}(\lambda)$ in deeper and larger blood vessels (>150 μm in diameter) requires using irradiation from therapeutic optical wavelength range (630–1100 nm) [8, 19].

In paper [16] both AMA and DMA were applied for the *in vitro* evaluation of blood absorption spectra in the wavelength range of 740–1040 nm. At the first step, reconstruction of $\mu_s'(\lambda)$ from OA measurements of $\mu_{eff}(\lambda)$ was performed for known $\mu_a(\lambda)$ of blood at different StO_2 levels. At the next step, using measured μ_{eff} spectra and reconstructed μ_s' spectra, relative concentrations of oxy- and deoxyhemoglobin (and therefore, blood oxygen saturation) was calculated using forward model of the absorbed energy distribution based on diffusion theory.

Different scientific groups perform OA measurements of StO_2 at various wavelengths combinations [10, 15, 18–22] depending on the laser source(s) and application. In case of the OA setup optimization by using limited number of wavelengths it is important to determine the optimal ones. In this relation, different methods of selection the optimal wavelength for OA measurements of StO_2 were proposed. In paper [23] the condition number of the absorption spectra matrix was implemented as an indicator of the stability for linear least squares spectral unmixing, and, as a result, for the four-wavelengths OA tomography measurements the following optimal wavelength ranges were proposed: around 650 nm, 700–750 nm, 800–920 nm, and 900–960 nm. In paper [24] an algorithm for optimal wavelength selection based on the Cramer–Rao lower bound for a two-layer (epidermis, dermis) skin model yielded a pair of optimal wavelengths near 600 nm for low blood content in skin, while increasing the blood content in the dermis gave a pair of 600 nm and 990 nm. In our previous work [8] we evaluated the optimal wavelengths for the two-wavelength OA measurements of StO_2 at various depths taking into account the acoustic pressure noise and the error in determination of optical scattering and absorption coefficients in numerical simulation. The results obtained in [8] indicate that the use of wavelengths less than 600 nm is inappropriate even at small depths due to extremely high signal attenuation. It was shown that the minimal error in the determination of StO_2 at depths from 2 to 8 mm can be achieved at the wavelengths of 658 and 1069 nm in the case of unknown (or partially known) spatial fluence distribution.

The main goal of the present work is to compare AMA and DMA for StO_2 determination from phantom, *in vitro* and *in vivo* data. For the first time, to our knowledge, spectra of optical absorption coefficient and effective optical attenuation coefficient were reconstructed in a rat *in vivo* simultaneously. The reconstructed spectra were matched with the corresponding published data for the range of physiological StO_2 values. Adequate *in vivo* saturation level was reconstructed using AMA, while calibration-free DMA failed to provide good reconstruction results. We demonstrate that the cost-efficiency of AMA can be increased by implementation of dual-wavelength probing scheme instead of multiple wavelength probing. We perform the analysis of the optimal wavelength pair within the range of 658–1069 nm which provide reconstruction of StO_2 value close to that derived from multiple wavelength measurements in the entire range.

2. Materials and methods

2.1. Determination of StO_2 from OA signal

2.1.1. Amplitude measurement approach (AMA). From OA measurements of pressure time series *p(t)* one can reconstruct the distribution of OA pressure local increment p_0 [Pa]. Pressure increment at the location $\mathbf{r}$ in the medium is generated as a result of absorption of a wide aperture illumination laser pulse at the wavelength λ [25]:

$$p_0(\mathbf{r}, \lambda) = \Gamma \mu_a(\mathbf{r}, \lambda) \Phi(\mathbf{r}, \lambda), \quad (1)$$

where μ_a [cm^{-1}] is the local optical absorption coefficient, Φ [mJ cm^{-2}] is the optical fluence, and Γ is the Grüneisen dimensionless parameter characterizing the efficiency of absorbed light conversion into ultrasound.

Absorption coefficient at the given point is related to the local concentrations of oxygenated (C_{HbO_2}) and deoxygenated (C_{Hb}) forms of hemoglobin:

$$\mu_a(\mathbf{r},\lambda) = C_{Hb}(\mathbf{r})\cdot\mu_a^{Hb}(\lambda) + C_{HbO_2}(\mathbf{r})\cdot\mu_a^{HbO_2}(\lambda), \quad (2)$$

where $\mu_a^{HbO_2}$ are the optical absorption coefficients of pure oxy- and deoxyhemoglobin. The map of μ_a can be extracted from $p_0(\mathbf{r}, \lambda)$ (equation (1)), which, in its turn, should be evaluated from the measured OA pressure *p(t)* using algorithms for acoustic reconstruction:

$$\mu_a(\mathbf{r},\lambda) = \frac{p_0(\mathbf{r},\lambda)}{\Gamma\Phi(\mathbf{r},\lambda)}. \quad (3)$$

Direct OA measurements of μ_a can be realized in superficial blood vessels using optical resolution OA microscopy [26] where optical fluence is considered constant. In other cases evaluation of μ_a map in accordance with equation (3) requires information about optical fluence distribution in biotissue [8]. In addition, precise calibration of the entire system should be applied to extract absolute values of μ_a required for accurate saturation determination. Equations (2) and (3) are the principal formulas of the AMA.

Because calculation of StO_2 requires knowing only two parameters (C_{HbO_2}, and C_{Hb}), the saturation map can be estimated from two-wavelengths OA measurements of μ_a by equations (2) and (3) [8]:

$$StO_2(\mathbf{r}) = \frac{C_{HbO_2}(\mathbf{r})}{C_{Hb}(\mathbf{r}) + C_{HbO_2}(\mathbf{r})} = \frac{\frac{p_0(\mathbf{r},\lambda_1)}{p_0(\mathbf{r},\lambda_2)}\cdot\frac{\Phi(\mathbf{r},\lambda_2)}{\Phi(\mathbf{r},\lambda_1)}\cdot\mu_2 - \mu_1}{\frac{p_0(\mathbf{r},\lambda_1)}{p_0(\mathbf{r},\lambda_2)}\cdot\frac{\Phi(\mathbf{r},\lambda_2)}{\Phi(\mathbf{r},\lambda_1)}\cdot\delta\mu_2 - \delta\mu_1}, \quad (4)$$

where $\mu_{1,2}$ are the optical absorption coefficients of pure deoxyhemoglobin at the wavelengths $\lambda_{1,2}$ and $\delta\mu_{1,2} = \mu_a^{Hb}(\lambda_{1,2}) - \mu_a^{HbO_2}(\lambda_{1,2})$ are the differences between the optical absorption coefficients of pure oxy- and deoxyhemoglobin at the wavelengths $\lambda_{1,2}$, $\Phi(\mathbf{r}, \lambda_{1,2})$ are the optical fluence values at the wavelengths $\lambda_{1,2}$.

2.1.2. Decay measurement approach (DMA). Under the assumptions blood is uniformly and diffusively scattering and illumination pattern is close to a plane wave, optical fluence in a blood vessel can be approximated by an exponential decay model described in [27]:

$$\Phi(\mathbf{r},\lambda) = \Phi_0\cdot k(\lambda)\cdot\exp(-\mu_{eff}(\mathbf{r},\lambda)\cdot z). \quad (5)$$

Here Φ_0 is the fluence at the object surface, and μ_{eff} is the effective attenuation coefficient implemented in the diffusion theory of light transport and related to the absorption coefficient μ_a and reduced scattering coefficient μ_s' [cm^{-1}] as:

$$\mu_{eff} = \sqrt{3\cdot\mu_a\cdot(\mu_a + \mu_s')}. \quad (6)$$

Backscattering coefficient k in equation (5) is described by an empirical formula [27]:

$$k = 3 + 5.4\cdot R_d - 2\cdot\exp(-17R_d), \quad (7)$$

where R_d is the total diffuse reflectance determined by μ_a and μ_s':

$$R_d = \exp\left(-\frac{8}{\sqrt{3\cdot\left(1+\frac{\mu_s'}{\mu_a}\right)}}\right). \quad (8)$$

Therefore, according to equation (1), OA signal detected from a vessel exponentially decays with the imaging depth z:

$$p_0(\mathbf{r},\lambda) = \Gamma\mu_a(\mathbf{r},\lambda)\Phi_0\cdot k(\lambda)\cdot\exp(-\mu_{eff}(\mathbf{r},\lambda)\cdot z). \quad (9)$$

Equations (6) and (9) allow indirect StO_2 estimation by evaluation of effective optical attenuation $\mu_{eff}(\lambda)$ from the slope of the detected OA signal [15, 16, 28] if μ_s' is known. Spectra of the reduced scattering coefficient of blood were reported and showed weak dependence on oxygen saturation [17]. Blood saturation is then estimated by variation of concentrations C_{HbO_2} and C_{Hb} in order to fit the blood absorption spectrum calculated from equation (2) to the experimental one derived from $\mu_{eff}(\lambda)$ measurements. This is the basis of the decay measurement approach (DMA) which does not require information of optical fluence distribution in the whole imaged object.

2.2. Phantom, in vitro and in vivo protocols

Test measurements of μ_{eff} spectra in the range of 532–1100 nm for a liquid phantom containing 0.36 vol% of black ink and 9.06 vol% of Intralipid 20%. To get statistically reliable data, measurements were repeated 3 times. Concentrations of black ink and Intralipid were chosen in order to design an optical phantom with the absorption and scattering properties mimicking typical optical properties of murine soft tissues in the considered spectral range [29, 30]. Optical properties of pure black ink and Intralipid were obtained from spectrophotometric measurements using Specord 250 PLUS spectrophotometer equipped with an integrating sphere (Analytik Jena, Germany). The values of $\mu_s'(\lambda)$ and $\mu_a(\lambda)$ were reconstructed from the measured diffuse transmittance and reflectance by inverse Monte Carlo technique [31]. Optical properties of the prepared phantom were also verified by the spectrophotometric measurements and inverse Monte Carlo reconstruction.

In vitro measurements were performed for a whole blood sample with Hct = 51%, $StO_2 = 1$. Fresh venous blood in the amount of 6 ml was taken from a healthy volunteer and then left in the open air to reach the required oxygenation. Oxygenation level was continuously controlled by an oxygen microsensor based on Clark OX-N electrode (Unisense, Denmark) and picoampermeter A2-4 (MNIPI, Belarus) for pO_2 measurements. In order to avoid coagulation, 10.8 mg of K_3EDTA was added to the sample. We performed three experiments for different thickness of blood sample: 2.76 mm, 3.28 mm and 4.96 mm. Optical properties of the 10-times diluted blood sample were evaluated using the described above spectrophotometric technique and then compared to the results of OA measurements. We also compared the OA-measured spectra of μ_{eff} and μ_a to the data published for Hct = 45% [32] and adapted for Hct = 51% according to the recalculation procedure [17].

I*n vivo* OA measurements were performed on the back vasculature of a 4 d old hairless rat. Before the investigation the rat was anaesthetized with an intraperitoneal injection of 50 mg kg^{-1} of Zoletil 100 and immobilized in prone position. The experiment was conducted on the lower thoracic spine. OA imaging was performed through the rat skin at a single position of the antenna. The experiment on animal was approved by the Local Ethic Committee of Privolzhsky Research Medical University (protocol # 4, 17.04.2018). All experiments were performed in accordance with the European Convention for the Protection of Vertebrate Animals used for Experimental and Other Scientific Purposes (ETS 123) and The Guide for the Care and Use of Laboratory Animals, 8th edition (NRC 2011, National Academic Press).

2.3. Experimental setup for phantom and in vitro OA measurements

Transmission-mode configuration of our OA measurement setup used for phantom and *in vitro* experiments is shown in figure 1(a) and is similar to that reported in [16]. A sample was illuminated from the top by a solid-state pulsed laser source LT-2214-PC (LOTIS TII, Belarus) with a pulse duration of 16 ns and 10 Hz pulse repetition rate. A custom-made 10:90 beam splitter with a calibrated pyroelectric sensor ES111C (Thorlabs, USA) was used to measure the energy of each laser pulse at the sample surface. We performed phantom and *in vitro* measurements at 21 wavelengths from the range of 532–1100 nm (532, 560, 565, 570, 575, 578, 584, 590, 596, 630, 640, 650, 658, 700, 760, 805, 850, 885, 900, 1064, 1069 nm). To measure $\mu_{\text{eff}}(\lambda)$ a custom-made ultrawideband ultrasonic detector (0.1–50 MHz at −30 dB level) based on polyvinylidene difluoride (PVDF) was employed.

2.4. Experimental setup for in vivo OA measurements

Reflection-mode configuration of OA measurements used for *in vivo* experiments is shown in figure 1(b) and is similar to the one reported in [33]. It provides a 2D OA tomography image (a B-scan) of *in vivo* rat back vasculature at each of 9 wavelengths in the range of 658–1100 nm (658, 700, 760, 805, 850, 885, 900, 950, 1069). Acquisition time of each B-scan is about a minute per each wavelength.

The studied object was illuminated from the top by a solid-state pulsed laser source LT-2214-PC (LOTIS TII, Belarus). Laser radiation was coupled into the fused end of the fiber bundle (Ceram Optec, Germany) with sixteen output arms. Each arm was 2.5 mm in diameter with a 0.17 numerical aperture in water. One output fiber was directed to the calibrated ES111C pyroelectric sensor (Thorlabs, USA) to measure energy of each laser pulse at the distal fiber tips. The energies of laser pulses at corresponding probing wavelengths registered by pyroelectric sensor are 450, 300, 297, 207, 128, 97, 126, 86, and 50 μJ. Fourteen output arms were placed at each of two sides of the linear detector array (LDA) unit and were directed onto the elevation focus (figure 1(b)). Sixteen ADC channels based on four NI5761 14-bit adapters (National Instruments, USA) were multiplexed with 64 elements of each LDA using 16 ADG711 switchers (Analog Devices, USA). The sample rate of A-scans was 125 MS s^{-1}. Ultrasound signals were registered by custom-made LDA L25-1 with 64 elements, 0.3 pitch and 25 mm elevation focus described in details in paper [33].

After measurements each B-scan of OA tomography data sets was processed by the reconstruction algorithm described in paper [34]. In order to account for non-uniform distribution of probing radiation within the object, OA signal was normalized in each image voxel for optical fluence calculated for typical optical properties of soft tissues in diffuse approximation [8].

3. Results

3.1. Phantom measurements

In the phantom study we performed evaluation of both $\mu_{\text{eff}}(\lambda)$ and $\mu_{\text{a}}(\lambda)$ with implementation of DMA and AMA, respectively. Figure 2(a) presents typical OA A-scans measured from the phantom. OA pressure signal at each optical wavelength was fitted by an exponential function (figure 2(a) black dashed lines). DMA-reconstructed spectra of μ_{eff} averaged over three equivalent OA measurements (figure 2(b) red line) are in good agreement with the spectrophotometry measurements of $\mu_{\text{eff}}(\lambda)$ (figure 2(b) blue line).

Spectra of μ_{a} were evaluated on the basis of AMA from equation (3), where OA signal amplitudes on the phantom surface corresponding to maxima of OA signals in figure 2(a) were normalized to laser energy and backscattering coefficient. The latter coefficient was calculated from equations (7) and (8) using μ_{a} and μ_{s}' data reconstructed from spectrophotometry measurements in the range of 532–1100 nm. Figure 2(c) demonstrates good agreement of the AMA-reconstructed spectra of μ_{a} averaged over three independent OA measurements (figure 2(c) red line) with the values reconstructed from spectrophotometry measurements (figure 2(c) blue line), except the region of 500–650 nm, where the OA signal amplitudes vary significantly from one experiment to another.

3.2. In vitro measurements

Figure 3(a) presents typical OA A-scans measured at two different wavelengths in whole blood of a healthy volunteer (Hct = 51%, $StO_2 = 1$). The results of DMA-reconstructed spectra of μ_{eff} in blood averaged for samples of different thicknesses (2.76 mm, 3.28 mm 4.96 mm) are demonstrated in figure 3(b). DMA-evaluated spectra of μ_{eff} are in good agreement with the μ_{eff} spectra reconstructed from spectrophotometry measurements for the diluted blood sample (figure 3(b) green line). However, we found the discrepancy of the measured $\mu_{\text{eff}}(\lambda)$ with the data published in [32] for $StO_2 = 1$, Hct = 45% but recalculated for Hct = 51% in accordance with [17, 32] (figure 3(b) red dashed line). Additionally, the spectrum from [32] was recalculated for the case of deoxygenated blood ($StO_2 = 0$) and plotted in figure 3(b) (blue

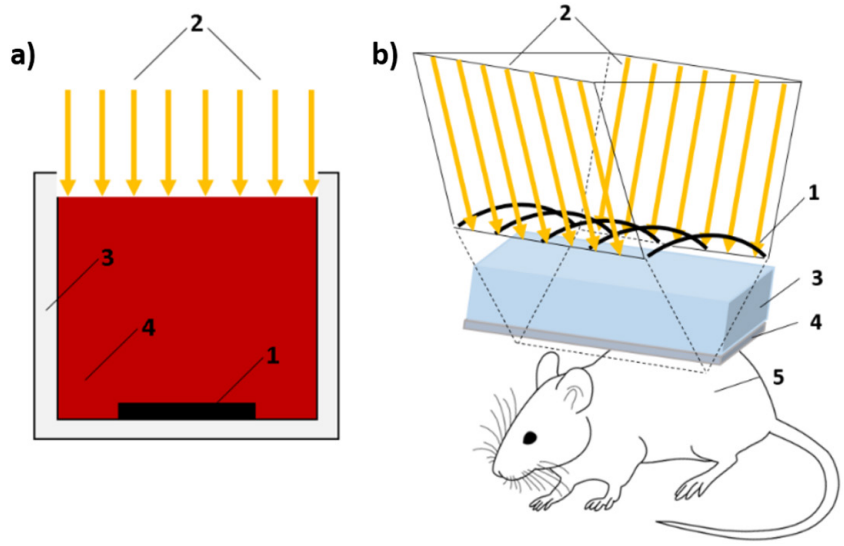

Figure 1. Schematic of OA measurement configuration: (a) for a phantom experiment: acoustic PVDF detector (1), plane wave illumination (2), cuvette (3), blood sample (4); (b) for *in vivo*: linear detector array L 25-1 (1), optical fibers (2), immersion chamber with water (3), ultrasound gel (4), object (5).

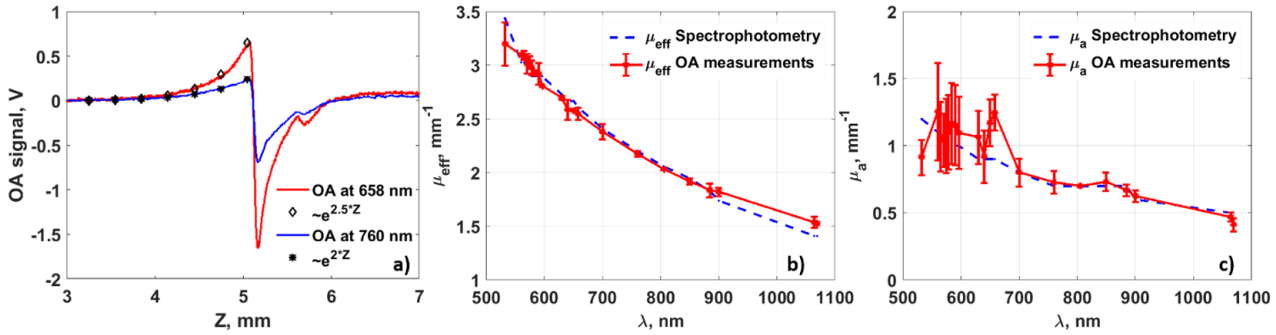

Figure 2. OA signals from a phantom at the wavelengths of 658 and 760 nm fitted by exponential functions (a); comparison of the averaged results of $\mu_{\text{eff}}(\lambda)$ reconstruction using DMA (b) and $\mu_a(\lambda)$ reconstruction using AMA (c) with the spectrophotometry measurements for the phantom.

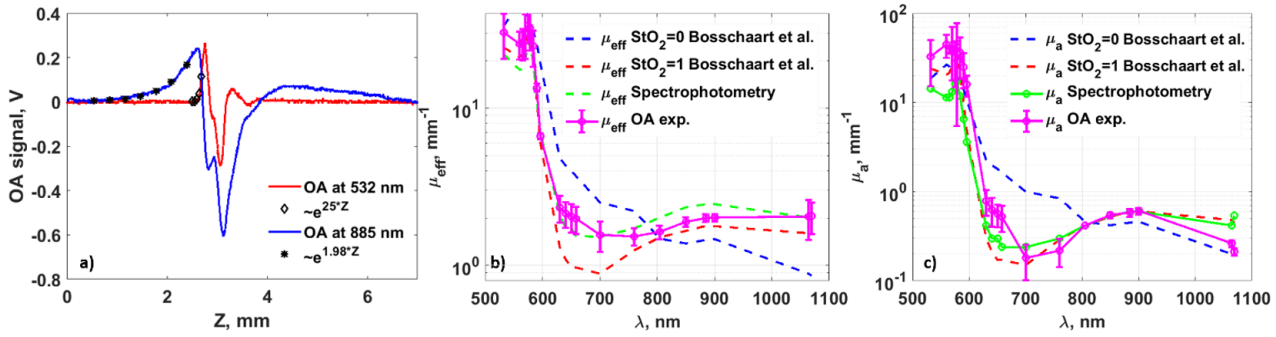

Figure 3. OA signals from a blood sample ($StO_2 = 1$) at the wavelengths of 532 and 885 nm fitted by exponential functions (a); comparison of the averaged results of $\mu_{\text{eff}}(\lambda)$ reconstruction using DMA (b) and $\mu_a(\lambda)$ reconstruction using AMA (c) with the spectrophotometry measurements for the blood sample and published data [32].

dashed line). One can see that in the range of 500–600 nm the confidence interval for the reconstructed values of μ_{eff} overlaps with the published μ_{eff} spectra both for $StO_2 = 1$ and $StO_2 = 0$. Therefore, accurate estimations of μ_{eff} cannot be performed in this range using our OA setup. However, the measurements in the range of 630–750 nm demonstrate high potential in StO_2 differentiation.

Using AMA, μ_a spectrum was calculated from equation (3) using the maximum value of OA A-scan (figure 3(a)). In transmission-mode the peak of A-scan comes from the surface of the object, therefore its value does not require depth-dependent fluence normalization, only normalization for laser energy and backscattering coefficient for each wavelength is required (equations (3) and (5)). Backscattering coefficient

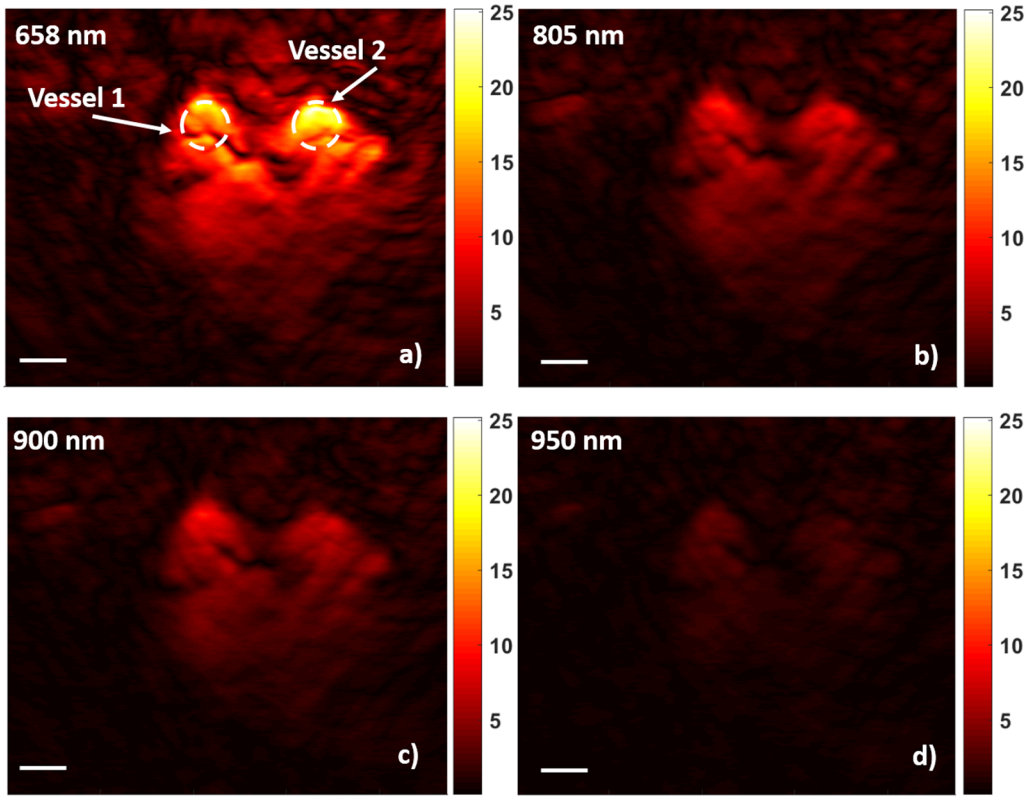

Figure 4. OA tomography B-scans reconstructed by SAFT + DCM at different laser wavelengths: (a) 658 nm; (b) 805 nm; (c) 900 nm; (d) 950 nm. The white dashed lines show the area containing blood vessels. Bar: 1 mm.

was calculated from equations (7) and (8) with optical properties taken from the paper [8] at different wavelengths in range of 532–1100 nm. Figure 3(c) shows evaluated μ_a spectrum of blood averaged over three OA measurements for samples of different thickness (figure 3(c) magenta line). It is in good agreement both with μ_a spectrum taken from the paper [32] for $StO_2 = 1$ (figure 3(c) red dashed line) and reconstructed from spectrophotometry measurements (figure 3(c) green line). The spectrum of μ_a for deoxygenated blood ($StO_2 = 0$) is given for a reference (figure 3(c) blue dashed line). The best match is observed in the wavelength range of 650–900 nm. However, similar to the estimates of μ_{eff}, in the wavelength range of 500–600 nm the reconstructed values of μ_a overlapped both with μ_a of deoxygenated and fully oxygenated blood.

3.3. In vivo measurements

Figure 4 presents OA tomography B-scans of a rat vasculature reconstructed by the recently developed SAFT + DCM approach with interpolation at different probing wavelengths. The SAFT+DCM approach combines traditional synthetic aperture focusing technique (SAFT) [35] with application of detection cone binary mask (DCM) limiting the contributing area by the geometrical shape of the ultrasonic detector spatial impulse response [34].

Two separate blood vessels can be easily distinguished in the reconstructed images (vessel 1 and vessel 2 in figure 4(a)). These two vessels anatomically correspond to two azygos and hemiazygos veins located bilaterally under the vertebral column [36]. The type of blood vessels can be determined more accurately by additional morphological studies.

Low signal-to-noise ratio (SNR) at the wavelengths larger than 950 nm is explained by small probing pulse laser energy at these wavelengths (figure 4(d)).

From the A-scans in the central cross-sections of blood vessels 1 (figure 5(a)) and 2 (figure 5(b)) we obtained the effective optical attenuation coefficient in the selected area (between black dashed lines in figures 5(a) and (b)) as a decay in exponential function at each of 9 wavelengths (figure 5(c), black lines). For comparison, the dependencies of μ_{eff} calculated from the published data [32] for different values of oxygenation in the range from 0 to 1 with a step of 0.1 are plotted in figure 5(c). The μ_{eff} confidence bounds defined by the slope variation in OA signal approximation are shown in figure 6(c). One can see that the trends of the reconstructed dependencies disagree with the data from [32] in the entire range of wavelengths. The largest discrepancy takes place at the wavelengths in the range of 950–1100 nm, where SNR is very small due to low laser pulse energy. The only acceptable match of our data with the data from [32] is observed at 658 nm for both vessels where the laser energy is the highest. As follows from [32], the values of μ_{eff} reconstructed at 658 nm correspond to StO_2 values of 0.44 and 0.41 for the vessels 1 and 2, respectively.

Since the accurate determination of the vessels boundaries in the B-scans is complicated, the further analysis is performed within the areas containing two blood vessels that are shown schematically in figure 4(a) by white dashed circles.

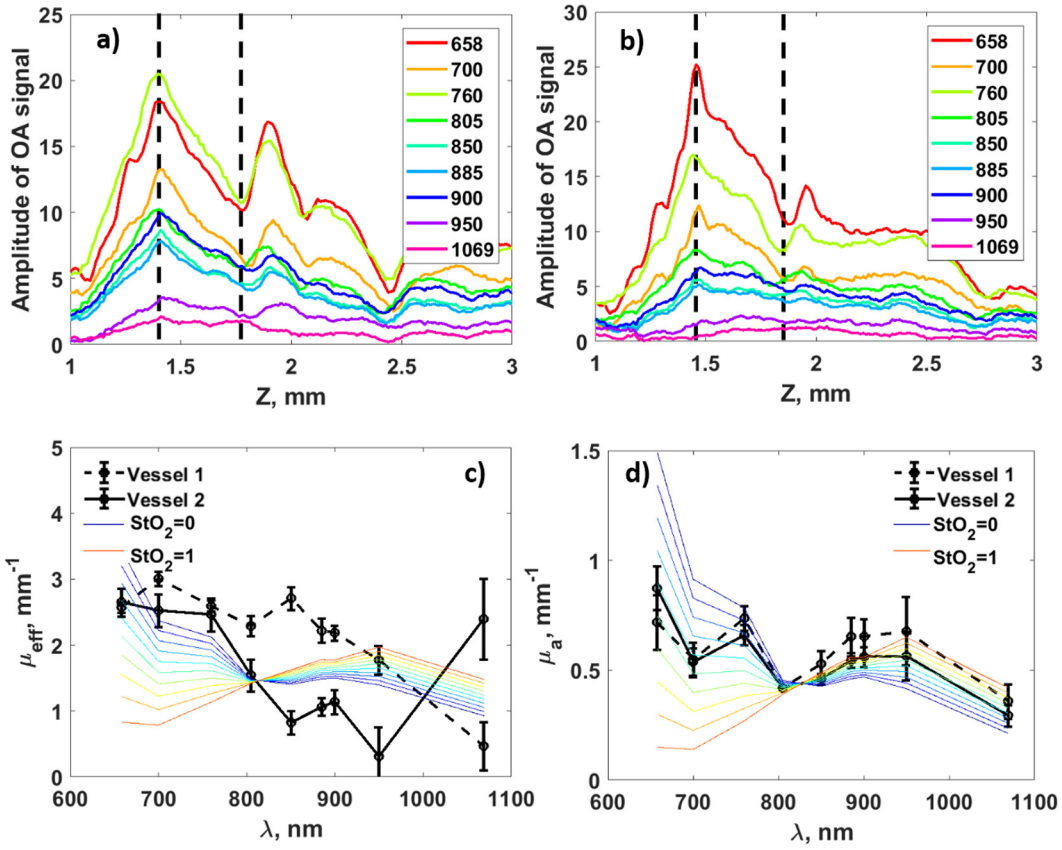

Figure 5. OA A-scans in the central cross-section of vessel 1 (a) and vessel 2 (b) in a rat for different probing wavelengths. Comparison of averaged μ_{eff} spectra estimated with the help of DMA (c) and averaged μ_{a} spectra estimated with the help of AMA (d) with μ_{eff} and μ_{a} spectra, respectively, calculated from the data in [32] for oxygenation values from 0 to 1 with a step of 0.1.

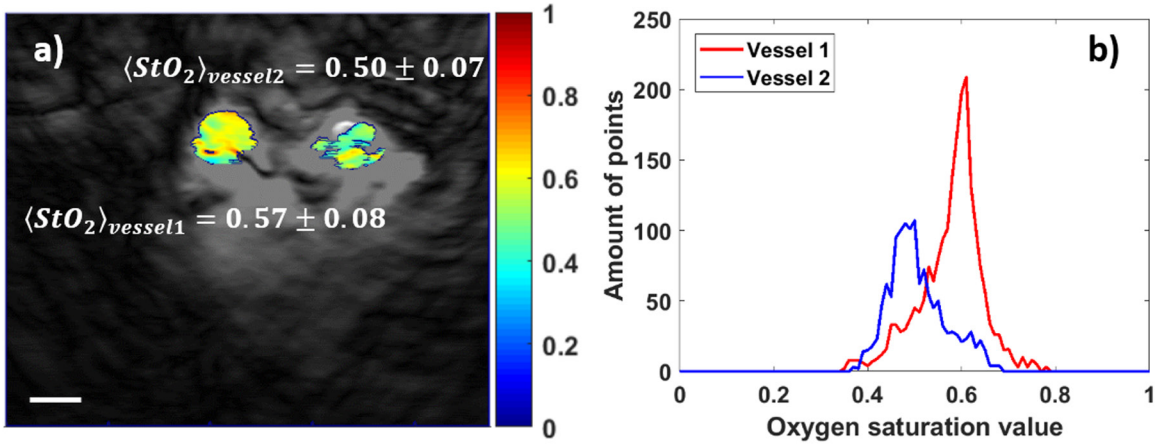

Figure 6. *In vivo* estimation of StO_2: (a) blood oxygen saturation map; (b) histogram of estimated saturation values in vessel 1 and vessel 2.

To evaluate absorption in each blood vessel from OA tomographic images (figure 4) using AMA, OA amplitudes were normalized for optical fluence at the current depth in the biotissue and for laser energy at the particular wavelength. Optical fluence dependence on depth was calculated according to equation (5) with μ_{eff} taken from [8]. Only the pixels with SNR $>$ 10 inside a vessel were taken into calculation and the obtained values of μ_{a} were average over these pixels for each of 9 wavelengths. Evaluated μ_{a} spectra are shown in figure 6(d) with the confidence bounds.

In order to estimate StO_2, we calculated the μ_{a} spectra from the data of [32] for different values of oxygenation from 0 to 1 with a step 0.1 and combined them with the evaluated spectra in one plot (figure 5(d), colored lines). One can see that the trend of the dependencies corresponds with the data from [32] in the entire wavelength range. We determined StO_2 value by fitting the experimental spectrum with the calculated one for saturation values ranging from 0 to 1 with a step of 0.01. The values of StO_2 averaged over the blood vessel area were estimated as 0.57 $\pm$ 0.08 and 0.50 $\pm$ 07 in vessel 1 and vessel 2,

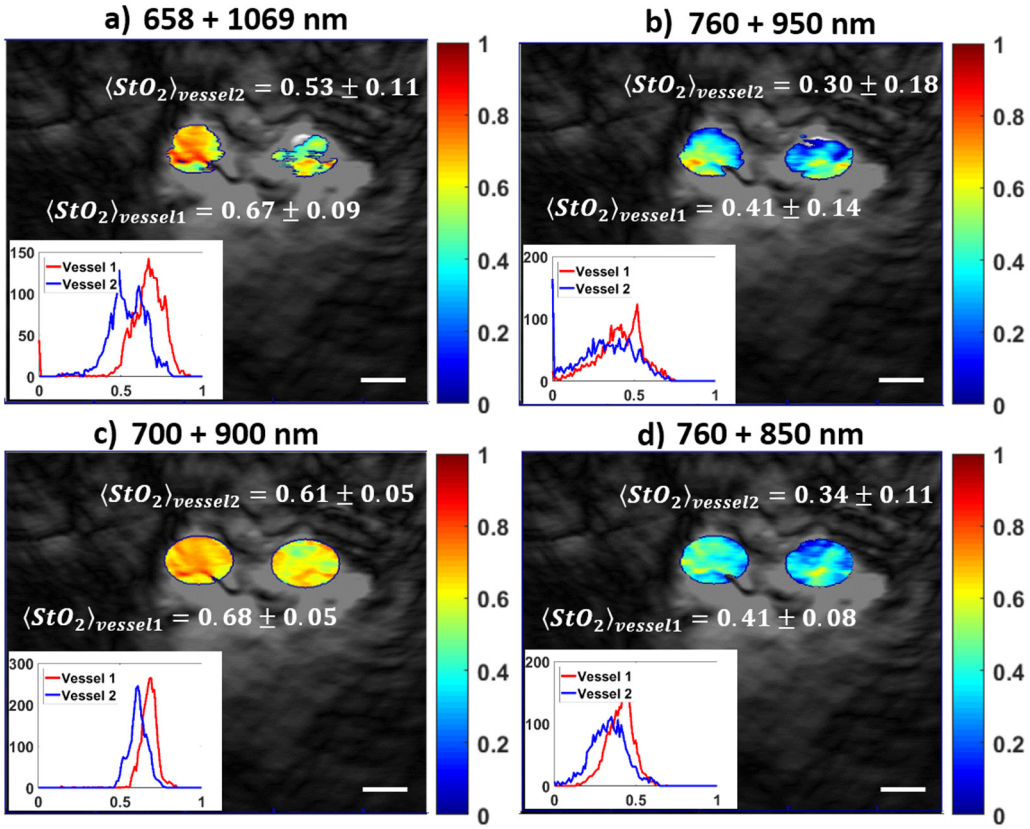

Figure 7. *In vivo* saturation maps of a rat back vasculature obtained from equation (4) using the following wavelengths: (a) 658 and 1069 nm; (b) 760 and 950 nm; (c) 700 and 900 nm; (d) 760 and 850 nm. The inlays show corresponding histograms of the saturation values in vessel 1 (red line) and vessel 2 (blue line).

Table 1. Average StO_2 level in vessel 1 (upper row) and vessel 2 (lower row) with its standard deviations (presented as $StO_2^{(I,II)}$ (λ_1, λ_2) $\pm$ $\sigma_{I,II}$ (λ_1, λ_2)) determined at different wavelengths pairs λ_1, λ_2. For non-physiological saturation values ($StO_2 < 0$, $StO_2 > 1$) dispersion values are omitted.

λ_2 \ λ_1		700	760	805	850	885	900	950	1069
8	65	>1	0.90 ± 0.04	0.68 ± 0.08	0.71 ± 0.06	0.75 ± 0.06	0.74 ± 0.06	0.68 ± 0.07	0.67 ± 0.09
		>1	0.77 ± 0.07	0.57 ± 0.08	0.56 ± 0.07	0.58 ± 0.06	0.60 ± 0.06	0.49 ± 0.13	0.53 ± 0.11
0	70	—	0.87 ± 0.07	0.57 ± 0.11	0.64 ± 0.05	0.68 ± 0.05	0.68 ± 0.05	0.60 ± 0.09	0.61 ± 0.09
			0.83 ± 0.10	0.58 ± 0.11	0.56 ± 0.08	0.59 ± 0.07	0.61 ± 0.05	0.49 ± 0.13	0.53 ± 0.12
0	76	—	—	0.16 ± 0.15	0.41 ± 0.08	0.50 ± 0.09	0.49 ± 0.09	0.41 ± 0.14	0.44 ± 0.13
				0.28 ± 0.10	0.34 ± 0.11	0.40 ± 0.12	0.42 ± 0.12	0.30 ± 0.18	0.40 ± 0.15
5	80	—	—	—	0.92 ± 0.42	>1	>1	0.71 ± 0.38	0.70 ± 0.29
					0.46 ± 0.28	0.62 ± 0.31	0.70 ± 0.38	0.36 ± 0.42	0.47 ± 0.36
0	85	—	—	—	—	>1	>1	>1	>1
						>1	<0	>1	>1
5	88	—	—	—	—	—	>1	0.16 ± 0.75	0.35 ± 0.70
							>1	0.08 ± 0.95	0.31 ± 0.98
0	90	—	—	—	—	—	—	0.20 ± 0.75	0.36 ± 0.70
								0.01 ± 0.86	0.29 ± 0.90
0	95	—	—	—	—	—	—	—	<0
									>1

respectively. The obtained results are in good agreement with the physiological values for venous blood oxygenation in a rat [37] equal to 0.57 ± 0.02. We also determined StO_2 value in each point of the considered blood vessels. The obtained saturation map together with the histogram of saturation distribution is shown in figure 6.

Multispectral OA measurements require expensive equipment, therefore reduction of the number of the probing

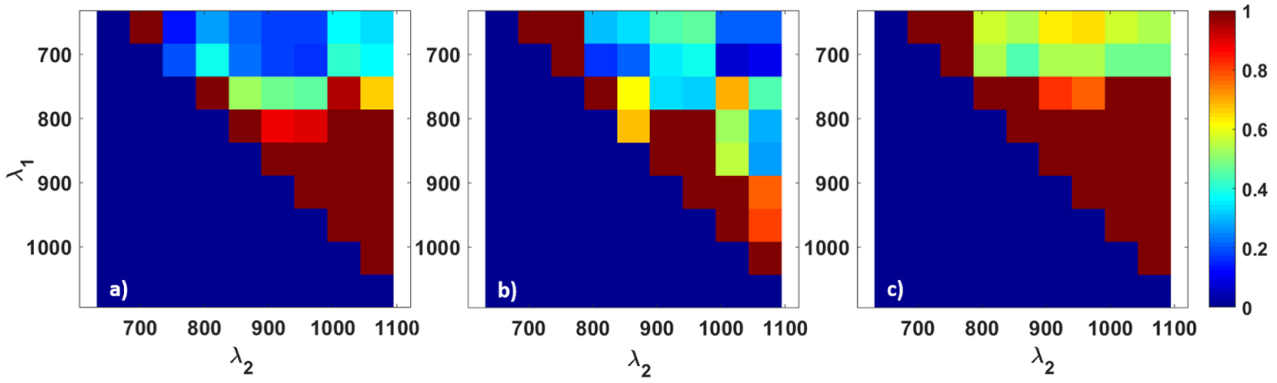

Figure 8. Diagrams of S_f representing StO_2 fluctuation (a), S_d representing value StO_2 deviation from the spectrally averaged value (b), and summarizing score S (c).

wavelengths is a promising way to a cost-effective technology. We estimated StO_2 value from equation (4) employing all available wavelength pairs from the entire set of probing wavelengths. Saturation values were calculated only for the pixels where the OA SNR exceeds 10 at the chosen pair of wavelengths. The obtained saturation maps superimposed on the corresponding grayscale OA B-scans are depicted in figure 7 together with the saturation distribution histograms.

Saturation values $\mathrm{StO}_2^{(\mathrm{I,II})}(\lambda_1, \lambda_2)$ calculated for vessels 1,2 for each wavelengths pair (λ_1, λ_2) and averaged over the vessel area are summarized in table 1 (vessel number is shown in Roman numerals). Since the *in vivo* saturation values in these vessels cannot be measured independently by another technique, the criteria for adequacy of the obtained results are based on the physiologic values typical for a rat veins and estimated as 0.57 ± 0.02 [37]. Another criterion is the agreement of the value derived by the wavelength pair with the value derived from the entire spectrum (depicted in figure 6).

However, for some pairs of wavelengths the values of StO_2 vary greatly within a vessel and differ significantly both from the averaged and the reference saturation [37] (see, for example, figure 7(b)). This indicates that these pairs of probing wavelengths are not valid for the reconstruction. Another criterion of the results adequacy can serve the dispersion of StO_2 values reconstructed by the pair of wavelengths from that reconstructed by the entire spectrum (figure 6(b)). The inlays in figure 7 demonstrate the histograms of StO_2 distribution in each vessel for the given wavelength pair. One can see that both the pair of [658 nm and 1069 nm] and [700 nm and 900 nm] provide StO_2 values which are close to each other and to physiological one (figures 7(a) and (c)); however, the standard deviation for the pair [700 nm and 900 nm] is much smaller which makes this pair more preferable for measurements with the given laser pulse energies. Standard deviation of saturation values $\sigma_{\mathrm{I}}(\lambda_1, \lambda_2)$ and $\sigma_{\mathrm{II}}(\lambda_1, \lambda_2)$ are summarized in table 1 within each vessel for each wavelength pair.

In order to find the optimal wavelengths pair which suits all the criteria discussed above we proposed a numerical score which is calculated as a sum of scores S_f and S_d responsible for particular criteria:

$$S = S_f + S_d = \left[\frac{|\sigma_{\mathrm{I}}(\lambda_1,\lambda_2)|}{\mathrm{StO}_2^{\mathrm{I}}(\lambda_1,\lambda_2)} + \frac{|\sigma_{\mathrm{II}}(\lambda_1,\lambda_2)|}{\mathrm{StO}_2^{\mathrm{II}}(\lambda_1,\lambda_2)}\right] + \left[\frac{\mathrm{StO}_2^{\mathrm{I}}(\lambda_1,\lambda_2) - \overline{\mathrm{StO}_2^{\mathrm{I}}}}{\overline{\mathrm{StO}_2^{\mathrm{I}}}} + \frac{\mathrm{StO}_2^{\mathrm{II}}(\lambda_1,\lambda_2) - \mathrm{StO}_2^{\mathrm{I,II}}\overline{\mathrm{StO}_2^{\mathrm{II}}}}{\overline{\mathrm{StO}_2^{\mathrm{II}}}}\right], \quad (10)$$

where $\sigma_{\mathrm{I,II}}(\lambda_1, \lambda_2)$ are the standard deviations of saturation values, $\mathrm{StO}_2^{\mathrm{I,II}}$ are the saturation values obtained from the entire spectrum and averaged over the respective vessel, $\mathrm{StO}_2^{\mathrm{I,II}}(\lambda_1, \lambda_2)(\lambda_1, \lambda_2)$ are the saturation values in vessels 1,2 (vessel number is shown in Roman numerals), respectively, for the considered wavelength pair. Scores S_f and S_d represent relative fluctuation of StO_2 value and deviation from the spectrally average StO_2 value, respectively, summed over both vessels for a given pair of wavelengths. Lesser values of the score indicate smaller discrepancy of the StO_2 value obtained for the considered wavelength pair from the average StO_2 value estimated for the whole spectral range and smaller variations of StO_2 level within the vessel.

Figure 8 demonstrates diagrams of scores S_f and S_d and the summarizing score S in dependence of both wavelengths λ_1 and λ_2. Diagrams for S_f and S_d criteria indicate that, in a pair of wavelengths minimizing each score, the first one should be chosen as 658 nm or 700 nm while the second one should be chosen from the range of 805–1069 nm. The summarizing score S confirms this conclusion while specifying that the most optimal wavelength pairs are 700 and a wavelength from the range of 850–1069 nm. Note that the values of optimal wavelengths in each found pair lie on opposite sides of the isosbestic point (near 805 nm [17]).

4. Discussion

In this study we compare two approaches to reconstruction of oxygen saturation from multispectral OA measurements: a calibration-free evaluation of the effective attenuation coefficient derived from in-depth OA signal decay (DMA) and determination of optical absorption coefficient from OA amplitudes (AMA). Both approaches were tested in phantom, *in vitro*, and *in vivo* experiments. Experiment with tissue-mimicking

phantoms demonstrated good agreement of the phantom optical properties reconstructed by both approaches with the values obtained from independent spectrophotometry measurements confirming the applicability of both techniques (figure 2). However, in *in vitro* experiment with blood sample DMA demonstrated much lower potential as compared to AMA (figure 3(b) versus (c)) due to large difference between experimentally obtained μ_{eff} spectra and the data from [32]. This discrepancy can be explained by the difference in properties of the blood samples in the compared experiments. The latter assumption is partially confirmed by agreement of μ_{eff} spectra obtained from OA measurements with those from spectrophotometry measurements. On the contrary, the μ_{a} spectra derived from OA amplitudes demonstrate good agreement both with spectrophotometric measurements and literature data (figure 3(c)) showing that employment of reconstructed μ_{a} values for determination of saturation is more preferable as compared to μ_{eff} values.

Similar to *in vitro* results, in *in vivo* measurements the reconstructed dependence of μ_{eff} differs significantly from the literature data in the entire range of wavelengths (figure 5(c)). Moreover, the μ_{eff} values for two veins differ from each other (up to 5 times), which is in contrary with the physiological principles. This discrepancy cannot be explained by the difference in reduced scattering coefficient of the blood from the literature data, since the observed blood vessels are the similar veins. The largest discrepancy takes place at the wavelengths in the range of 950–1100 nm, where the signal-to-noise ratio is very small due to low laser pulse energy. The only reasonable result for both vessels is observed at 658 nm where the laser pulse energy is maximal. The values of μ_{eff} reconstructed at 658 nm correspond to 0.44 and 0.41 saturation values for vessel 1 and vessel 2, respectively.

Moreover, DMA yields a μ_{eff} value averaged over the in-depth region where the signal decay is fitted, while AMA gives a saturation map providing a μ_{a} value in each point where the OA signal-to-noise ratio is sufficient. The above-mentioned drawbacks of DMA make AMA more preferable for *in vivo* estimations of blood saturation although the latter needs accounting for optical fluence.

The study results demonstrate for StO_2 determination from μ_{eff} using DMA, a high signal-to-noise ratio is required, which can be achieved in large blood vessels, preferably by using high numerical aperture detectors or/and high energy of laser pulses. In particular, this technique has high potential to determine StO_2 in deep single vessels, where AMA gives a large error associated with the assessment of the optical fluence at depths. However, for 2D or 3D OA visualization of surface vessels (at the depth of a few millimeters), AMA is more preferable, since in this imaging area the blood vessels' diameters are usually small. In our *in vivo* experiments the increase of optical fluence within the limits permitted by ANSI Z136.1 standard for laser safety can enhance the signal-to-noise ratio, and, hence, the accuracy of StO_2 measurements.

For blood vessels adjacent to each other in a lateral direction (figure 4(a)), the simple method of exponential fluence compensation applied to OA data gives good results. However, in case of two blood vessels arranged one above the other in the axial direction the exponential compensation will lead to an inaccurate estimate of StO_2 for the lower vessel. This is connected with the strong fluence attenuation in the upper blood vessel. Therefore, the optical fluence will demonstrate complicated depth-dependence. Note, that in the therapeutic transparency window of 650–1100 nm the blood absorption coefficient is relatively small and, therefore, the effect of shadows from superficial blood vessels is minimized [8]. Thus, the contribution of superficial microvascular bed to attenuation of optical fluence does not strongly affect its general exponential shape.

The calculations of μ_{a} spectra from OA signal amplitudes for both *in vivo* and *in vitro* experiments demonstrated that the dependencies trend correspond to that for the literature data. The best match for *in vitro* measurements (figure 3(c)) is observed in the wavelength range of 650–900 nm, however, similar to the estimates of μ_{eff}, in the wavelength range of 500–600 nm the reconstructed values of μ_{a} for $StO_2 = 1$ overlap with literature data both for deoxygenated and fully oxygenated blood. Hence, this wavelength range should not be used in our setup for accurate measurements of blood oxygen saturation.

From *in vivo* measurements and AMA, StO_2 can be determined by fitting the experimentally measured μ_{a} spectrum with a spectrum for particular saturation derived from the literature data. In the obtained OA B-scan for two veins of the rat thoracic spine the obtained StO_2 values are 0.57 ± 0.08 and 0.50 ± 0.07 (figure 6(a)). These values are close to each other and are in good agreement with physiological values for venous blood oxygenation in a rat [37], that amounts 0.57 ± 0.02. The obtained StO_2 values are also within the physiological range of venous blood oxygenation [38, 39].

From figure 5(d) one can see that the measured μ_{a} spectrum for vessel 1 differs from the all curves derived from literature data, nevertheless, the difference between the reconstructed μ_{a} spectra in two vessels lie within the confidence bounds of the measured value. Most likely, the variations of the OA signal for particular wavelengths are associated with insufficiently accurate normalization to the laser pulse energy, originating from the change in the laser beam shape at the OPO laser output as a result of wavelength tuning. The change in the beam shape may affect the distribution of intensity at the entrances of both the reference fiber bundle where the reference pulse energy is measured for normalization, and the object fiber bundle that delivers probing radiation to the object. The elimination of this drawback (the use of lasers with a more stable output beam shape, the use of an optical homogenizer, etc) is likely to increase the accuracy of the obtained value. Another possible reason of inaccuracy consists in a laboratory animal breathing that also may lead to variations of saturation values in a vein during measurement.

To increase the cost efficiency of the proposed technique, a pair of probing wavelength can be employed for OA measurements instead of multiple wavelength measurements providing a μ_{a} spectrum. We demonstrated that the optimal wavelength pairs are 700 nm and a wavelength from the range [850 nm, 1069 nm]. The values of optimal wavelengths in each found pair lie on opposite sides of the isosbestic point (near

805 nm). Unfortunately, the employed laser source provides low energy of the probing pulse at the wavelength of 1069 nm, hence, lower wavelengths are preferable for measurements. Employment of the pair [700 nm, 900 nm] yields the values of 0.68 ± 0.05 and 0.61 ± 0.05 for vessel 1 and vessel 2, respectively. These results are in good agreement with our previous prediction [8] that employment of this wavelength pair gives an error of 5% in saturation determination when the optical properties are approximately known.

5. Conclusion

We report on the comparison of two approaches to the reconstruction of oxygen saturation within blood vessels from multispectral OA measurements: a spatially-resolving approach based on determination of absorption coefficient from OA signal amplitudes, and a calibration-free approach based on evaluation of effective optical attenuation coefficient from the in-depth OA signal decay. Both approaches were verified in phantom, *in vitro* and *in vivo* measurements. For the first time, to our knowledge, spectra of optical absorption coefficient and effective optical attenuation coefficient were reconstructed in a rat *in vivo* simultaneously. The results of μ_a spectra reconstruction from the *in vitro* and *in vivo* measurements of OA amplitudes demonstrate good agreement with the published data, while calibration-free approach based on signal decay measurements failed to provide good correspondence with the literature data. This indicates that the first reconstruction approach is preferable for the *in vivo* determination of StO_2 as compared to the second approach. Reconstruction of blood oxygen saturation from the *in vivo* measured OA signal amplitudes in a rat yields the values of 0.57 ± 0.08 and 0.50 ± 0.07 for the two vessels which is in good agreement with the physiological values. We demonstrate that for cost-effective measurements a dual-probing wavelength scheme can be employed instead of multiple wavelength probing. We found that the wavelength of 700 nm combined with a wavelength from the range of 850–1069 nm provides reconstructed saturation values close to the reference ones derived from multiple wavelength measurements in the entire range of 658–1069 nm.

Acknowledgments

The work was supported by the Russian Science Foundation, project no. 18-45-06006 and the Helmholtz-RSF joint research Grant No. HRSF-0020. The authors would like to thank the staff of the IAP RAS, Mr M Prudnikov and Mr V Vorobyev for the development of detector array.

The authors declare that there are no conflicts of interest related to this article.

References

[1] Garcia-Uribe A, Erpelding T N, Krumholz A, Ke H, Maslov K, Appleton C, Margenthaler J A and Wang L V 2015 Dual-modality photoacoustic and ultrasound imaging system for noninvasive sentinel lymph node detection in patients with breast cancer *Sci. Rep.* **5** 15748

[2] Taruttis A and Ntziachristos V 2015 Advances in real-time multispectral optoacoustic imaging and its applications *Nat. Photon.* **9** 219

[3] Deán-Ben X L and Razansky D 2013 Functional optoacoustic human angiography with handheld video rate three dimensional scanner *Photoacoustics* **1** 68–73

[4] Lan B, Liu W, Wang Y-C, Shi J, Li Y, Xu S, Sheng H, Zhou Q, Zou J and Hoffmann U 2018 High-speed widefield photoacoustic microscopy of small-animal hemodynamics *Biomed. Opt. Express* **9** 4689–701

[5] Rebling J, Estrada H, Gottschalk S, Sela G, Zwack M, Wissmeyer G, Ntziachristos V and Razansky D 2018 Dual-wavelength hybrid optoacoustic-ultrasound biomicroscopy for functional imaging of large-scale cerebral vascular networks *J. Biophotonics* **11** e201800057

[6] Subochev P, Orlova A, Smolina E, Kirillov A, Shakhova N and Turchin I 2018 Raster-scan optoacoustic angiography reveals 3D microcirculatory changes during cuffed occlusion *Laser Phys. Lett.* **15** 045602

[7] Guo Z, Favazza C P, Garcia-Uribe A and Wang L V 2012 Quantitative photoacoustic microscopy of optical absorption coefficients from acoustic spectra in the optical diffusive regime *J. Biomed. Opt.* **17** 066011

[8] Perekatova V, Subochev P, Kleshnin M and Turchin I 2016 Optimal wavelengths for optoacoustic measurements of blood oxygen saturation in biological tissues *Biomed. Opt. Express* **7** 3979–95

[9] Kirillin M, Perekatova V, Turchin I and Subochev P 2017 Fluence compensation in raster-scan optoacoustic angiography *Photoacoustics* **8** 59–67

[10] Sivaramakrishnan M, Maslov K, Zhang H F, Stoica G and Wang L V 2007 Limitations of quantitative photoacoustic measurements of blood oxygenation in small vessels *Phys. Med. Biol.* **52** 1349

[11] Turner J, Estrada H, Kneipp M and Razansky D 2017 Universal weighted synthetic aperture focusing technique (W-SAFT) for scanning optoacoustic microscopy *Optica* **4** 770–8

[12] Bauer A Q, Nothdurft R E, Erpelding T N, Wang L V and Culver J P 2011 Quantitative photoacoustic imaging: correcting for heterogeneous light fluence distributions using diffuse optical tomography *J. Biomed. Opt.* **16** 096016

[13] Ulrich L, Ahnen L, Akarçay H G, Sanchez S, Jaeger M, Held G, Wolf M and Frenz M 2018 Spectral correction for handheld optoacoustic imaging by means of near-infrared optical tomography in reflection mode *J. Biophotonics* **12** e201800112

[14] Laufer J, Delpy D, Elwell C and Beard P 2006 Quantitative spatially resolved measurement of tissue chromophore concentrations using photoacoustic spectroscopy: application to the measurement of blood oxygenation and haemoglobin concentration *Phys. Med. Biol.* **52** 141

[15] Guo Z, Favazza C, Garcia-Uribe A and Wang L V 2012 Quantitative photoacoustic microscopy of optical absorption coefficients from acoustic spectra in the optical diffusive regime *J. Biomed. Opt.* **17** 0660111

[16] Laufer J, Elwell C, Delpy D and Beard P 2005 *In vitro* measurements of absolute blood oxygen saturation using pulsed near-infrared photoacoustic spectroscopy: accuracy and resolution *Phys. Med. Biol.* **50** 4409

[17] Roggan A, Friebel M, Dörschel K, Hahn A and Mueller G J 1999 Optical properties of circulating human blood in the wavelength range 400–2500 nm *J. Biomed. Opt.* **4** 36–47

[18] Zhang H F, Maslov K, Sivaramakrishnan M, Stoica G and Wang L V 2007 Imaging of hemoglobin oxygen saturation

variations in single vessels *in vivo* using photoacoustic microscopy *Appl. Phys. Lett.* **90** 053901
[19] Petrov I, Petrov Y, Prough D, Cicenaite I, Deyo D and Esenaliev R 2012 Optoacoustic monitoring of cerebral venous blood oxygenation though intact scalp in large animals *Opt. Express* **20** 4159–67
[20] Chen Z, Yang S and Xing D 2012 *In vivo* detection of hemoglobin oxygen saturation and carboxyhemoglobin saturation with multiwavelength photoacoustic microscopy *Opt. Lett.* **37** 3414–6
[21] Ning B, Kennedy M J, Dixon A J, Sun N, Cao R, Soetikno B T, Chen R, Zhou Q, Shung K K and Hossack J A 2015 Simultaneous photoacoustic microscopy of microvascular anatomy, oxygen saturation, and blood flow *Opt. Lett.* **40** 910–3
[22] Petrova I, Petrov Y, Esenaliev R, Deyo D, Cicenaite I and Prough D 2009 Noninvasive monitoring of cerebral blood oxygenation in ovine superior sagittal sinus with novel multi-wavelength optoacoustic system *Opt. Express* **17** 7285–94
[23] Xiao J, Yuan Z, He J and Jiang H 2010 Quantitative multispectral photoacoustic tomography and wavelength optimization *J. X-Ray Sci. Technol.* **18** 415–27
[24] Modgil D and La Riviére P J 2010 Optimizing wavelength choice for quantitative optoacoustic imaging using the Cramer–Rao lower bound *Phys. Med. Biol.* **55** 7231
[25] Cox B, Laufer J G, Arridge S R and Beard P C 2012 Quantitative spectroscopic photoacoustic imaging: a review *J. Biomed. Opt.* **17** 0612021
[26] Hu S, Maslov K and Wang L V 2011 Second-generation optical-resolution photoacoustic microscopy with improved sensitivity and speed *Opt. Lett.* **36** 1134–6
[27] Jacques S L 2010 How tissue optics affect dosimetry of photodynamic therapy *J. Biomed. Opt.* **15** 051608–6
[28] Petrov Y Y, Petrova I Y, Patrikeev I A, Esenaliev R O and Prough D S 2006 Multiwavelength optoacoustic system for noninvasive monitoring of cerebral venous oxygenation: a pilot clinical test in the internal jugular vein *Opt. Lett.* **31** 1827–9
[29] Loginova D A, Sergeeva E A, Krainov A, Agrba P D and Kirillin M Y 2016 Liquid optical phantoms mimicking spectral characteristics of laboratory mouse biotissues *Quantum Electron.* **46** 528
[30] Mesradi M, Genoux A, Cuplov V, Abi-Haidar D, Jan S, Buvat I and Pain F 2013 Experimental and analytical comparative study of optical coefficient of fresh and frozen rat tissues *J. Biomed. Opt.* **18** 117010
[31] Skobelkina A V *et al* 2018 Photoluminescence and optical properties of nanoparticles formed via laser ablation of porous silicon *Memoirs of the Faculty of Physics* p 1841302
[32] Bosschaart N, Edelman G J, Aalders M C, van Leeuwen T G and Faber D J 2014 A literature review and novel theoretical approach on the optical properties of whole blood *Lasers Med. Sci.* **29** 453–79
[33] Subochev P, Prudnikov M, Vorobyev V, Postnikova A, Sergeev E, Perekatova V, Orlova A, Kotomina V and Turchin I 2018 Wideband linear detector arrays for optoacoustic imaging based on polyvinylidene difluoride films *J. Biomed. Opt.* **23** 091408
[34] Perekatova V V, Kirillin M Y, Turchin I V and Subochev P V 2018 Combination of virtual point detector concept and fluence compensation in acoustic resolution photoacoustic microscopy *J. Biomed. Opt.* **23** 091414
[35] Li M-L, Zhang H F, Maslov K, Stoica G and Wang L V 2006 Improved *in vivo* photoacoustic microscopy based on a virtual-detector concept *Opt. Lett.* **31** 474–6
[36] Halpern M H 1953 The azygos vein system in the rat *Anatomical Rec.* **116** 83–93
[37] Rohlicek C, Matsuoka T and Saiki C 2002 Cardiovascular response to acute hypoxemia in adult rats hypoxemic neonatally *Cardiovasc. Res.* **53** 263–70
[38] Roddie I, Shepherd J and Whelan R 1956 Evidence from venous oxygen saturation measurements that the increase in forearm blood flow during body heating is confined to the skin *J. Physiol.* **134** 444–50
[39] Li M, Tang Y and Yao J 2018 Photoacoustic tomography of blood oxygenation: a mini review *Photoacoustics* **10** 65–73